Exploring the Potential of AlphaFold Distograms for Predicting Binding-induced Hinge Motions

Büşra Savaş[1,2], Ayşe Berçin Barlas[1,2], Ezgi Karaca[1,2]

[1]İzmir Biomedicine and Genome Center, İzmir, Türkiye; [2]Izmir International Biomedicine and Genome Institute, Dokuz Eylül University, Izmir, Türkiye

Corresponding Author: Ezgi Karaca (ezgi.karaca@ibg.edu.tr)

Abbreviation List

AF: AlphaFold

AIFM1: Apoptosis-Inducing Factor Mitochondrial 1

AK2: Adenylate Kinase 2

α-helix: Alpha helix

β: Beta

CAPRI: Critical Assessment of Predicted Interactions

Cβ: Beta carbon atom

cryo-EM: cryo-electron microscopy

DMPFold: DeepMetaPSICOV FolD

EIF2B3: Eukaryotic Translation Initiation Factor 2B Subunit 3

IDP: Intrinsically Disordered Protein

IL1R1: Interleukin-1 Receptor Type 1

MD: Molecular Dynamics

MIA40: Mitochondrial Intermembrane Space Import and Assembly Protein 40

MSA: Multiple Sequence Alignment

PAE: Predicted Aligned Error

PDB: Protein Data Bank

pLDDT: Predicted Local Distance Difference Test

pTM: Predicted TM-Score

RMSD: Root Mean Square Deviation

SI: Supplementary Information

Å: Ångström

Running Heading:

Predicting Hinge Motions with AlphaFold Distograms

Abstract

AlphaFold models provide static structural predictions, limiting their use in interpreting flexible regions in low-resolution cryo-EM maps. To address this, we assess whether AlphaFold-generated inter-residue distance probability distributions (distograms) can reveal conformational flexibility, focusing on binding-induced hinge motions. For this, we examine the AIFM1/AK2 complex, a metabolic assembly essential for ATP homeostasis. Molecular dynamics simulations and cryo-EM data reveal a hinge motion in AK2 upon AIFM1 binding. Strikingly, this motion is reflected in the distograms of apo AK2 generated by AlphaFold2 and AlphaFold3, although it is absent from their predicted structures. By extending this approach to additional systems, we show that distograms may offer a promising structure-free method to detect binding-induced hinge motions in flexible cryo-EM regions.

Key words: AlphaFold, Distogram, Conformational flexibility, Binding-induced hinge motion, Multiple sequence alignment

Word count: 117

Introduction

Before the AlphaFold2 (AF2) revolution, modeling protein interactions within low-resolution cryo-electron microscopy (cryo-EM) maps predominantly relied on integrative structural biology approaches [1–5]. The use of AF2 significantly advanced this process by enabling the fitting of accurate structure predictions into cryo-EM maps [6-8]. Despite these advances, AF2's utility remains limited when it comes to interpreting ambiguous regions in cryo-EM densities, caused by conformational flexibility [7, 9–12]. This is particularly pronounced in metabolic complexes, where functional transitions often involve hinge motions upon partner binding [6, 13-21]. To address this drawback, several recent methods have sought to repurpose AF2 as a conformational sampler [22–26]. One class of such methods manipulates the input multiple sequence alignment (MSA) while masking specific residue positions (columns) or entire sequences (rows) to encourage alternative conformational sampling [27,28]. Another strategy uses template-based guidance, where homologous structures from distinct functional states are used to steer predictions toward open or closed conformations [29,30]. Though, both strategies face practical limitations: MSA manipulation can lead to sampling of non-physiological conformations and appropriate templates are often unavailable. Moreover, these methods lack an intrinsic mechanism to evaluate which conformation best represents the biologically relevant state.

Before AF2's widespread use, another source to explore protein flexibility was proposed by Schwarz *et al.*. In 2021, they demonstrated that conformational variability at the residue level could be inferred from the shape of inter-residue distance probability distributions, known as distograms [31]. Introduced in CASP13 by AlphaFold1, distograms provide probabilistic distance profiles between all residue pairs [32]. Using DMPFold to generate distograms, Schwarz *et al.* demonstrated that residue pairs with known conformational variability exhibited multimodal distance distributions, while rigid regions showed unimodal sharp peaks [31,33]. These findings suggest that the number and shape of peaks in a distogram may serve as practical indicators of conformational flexibility, while utilizing the full MSA information. Building on this insight, we investigated whether distograms generated by AF2 and AF3 can hint at binding-induced hinge motions, an integral change in metabolic complexes.

To explore this hypothesis, we selected a recent cryo-EM structure of a complex formed between adenylate kinase 2 (AK2) and apoptosis-inducing factor mitochondria-associated 1 (AIFM1) as a test case [34]. This key mitochondrial assembly is involved in apoptotic signaling and ATP homeostasis. This system serves as an ideal proof-of-concept, as AK2 undergoes a distinct binding-induced hinge motion not observed in other adenylate

kinases. Here, we combined AF modeling with molecular dynamics (MD) simulations to compared predicted and observed inter-residue distance probability distributions, focusing on hinge-based flexibility [7,35]. To evaluate the broader applicability of this approach, we extended our analysis to three additional protein systems that may undergo binding-induced hinge motions as well.

Collectively, our findings provide preliminary yet promising evidence that AF-generated distogram profiles can serve as effective, structure-free indicators of hinge-based motions, potentially aiding in the interpretation of ambiguous regions in cryo-EM maps of metabolic complexes.

Results

A Key Metabolic Complex as a Proof-of-Concept for Distogram-Based Hinge Motion Prediction

AK2 is a mitochondrial isoform of the adenylate kinase enzyme family, responsible for maintaining cellular energy homeostasis. It catalyzes the reversible phosphorylation of AMP to ADP by using ATP [36,37]. With this, AK2 controls adenine nucleotide levels in the intermembrane space. By interacting with AIFM1, AK2 modulates redox-sensitive conformation of AIFM1, acting as a molecular switch between metabolic homeostasis and caspase-independent cell death [36-40]. Beyond its well-characterized domain motions, AK2 also exhibits a binding-induced hinge motion not captured in the previously resolved structures of this family. Two recent cryo-EM structures of the human AIFM1/AK2 complex reveal that the flexible C-terminal region of AK2, which is absent in the crystal structure of apo AK2 (PDB ID: 2C9Y), adopt a β-strand stacking against the C-terminal domain of AIFM1 [34,41,42]. In one of these structures, Schildhauer *et al*. used AF3 to model the complex and successfully fit the predicted β-strand interaction into their EM density (PDB ID: 9FL7; overall resolution: 4.3 Å; local resolution at the stacking site: ~5 Å) [34]. This finding was independently validated by Rothemann *et al.*, where the last eight C-terminal residues of AK2 are resolved, forming the β-stacking interface (PDB ID: 9GR0; overall resolution: 2.6 Å; local resolution: up to 3.2 Å)[41].

The unique C-terminal rearrangement observed in AK2 presents an unexplored opportunity to evaluate whether this specific binding-induced hinge motion can be captured by different AF versions. Expanding on this, we researched initially how AF3 handles the flexible C-terminal region of AK2 and observed that AF3 predicted it as an α-helix with low confidence, reflected by a mean pLDDT score of 54 (Figure 1A) Furthermore, AK2's PAE (predicted alignment error) matrix revealed that this C-terminal segment behaves as an independently moving domain (Figure S1). As it was already reported, AF3 modeled the C-terminal β-strand stacking against AIFM1 with high confidence (mean pLDDT: 77.6; Figure 1B) [34]. A comparison of the predicted apo and holo models revealed a substantial conformational shift at the C-terminus, with a root mean square deviation (RMSD) of 12 Å across the terminal residues. In particular, the Cβ–Cβ distance between residues 230 and 233 increased from 6.2 Å in the apo model to 10.5 Å in the holo model, capturing a key hinge-driven rearrangement observed in the AIFM1/AK2 complex. Because this distance best reflects our focus on binding-induced conformational change (Figure S2), we use the 230–233 residue pair as a marker to track this hinge motion throughout the study.

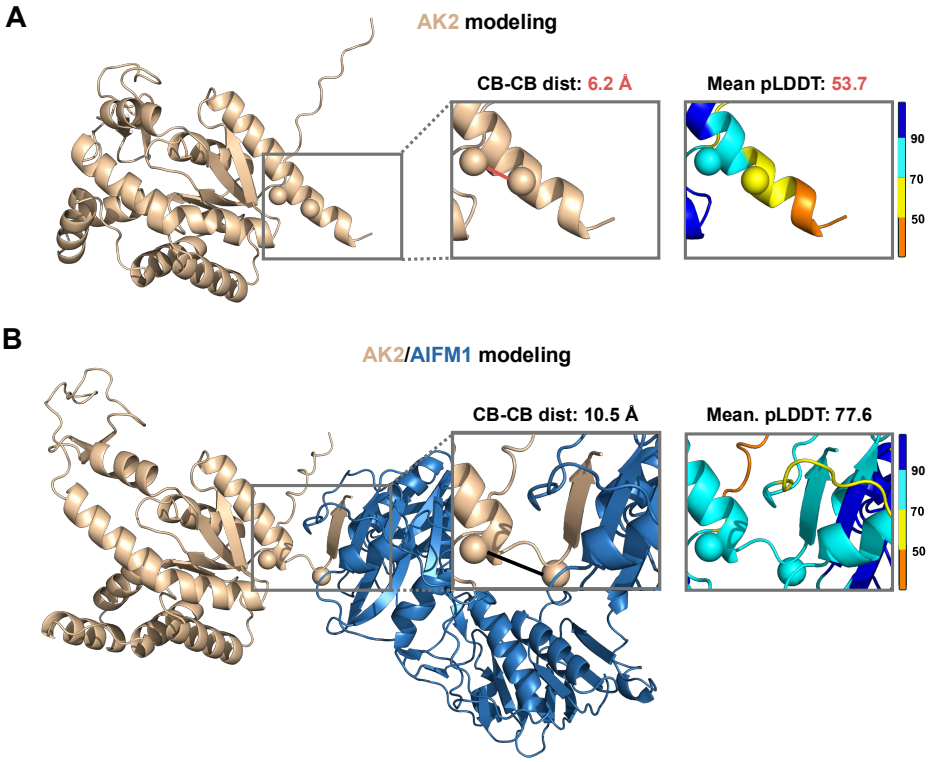

Figure 1. AlphaFold3 models capture a hinge-driven conformational switch of AK2. Top-ranked AF3 predictions (among 25 models) for apo **(A)** and holo **(B)** states of AK2 are shown. AK2 is depicted in wheat and AIFM1 in blue**.** Residues 230 and 233 of AK2, located at the flexible C-terminal end, are highlighted as spheres. Insets show close-up views of the Cβ–Cβ marker distance, together with the mean Cβ pLDDT scores of the last ten residues. pLDDT coloring indicates model confidence, with blue representing high and orange low confidence.

As a reference for ground truth, we monitored the marker distance between residues 230 and 233 with MD simulations. For the holo state, we relied on the previously published 4 μs all-atom MD trajectories of the AIFM1/AK2 complex (Figure S3) [34,43]. To provide a comparative baseline, we conducted 4 μs of MD simulations for apo AK2 using the same protocol described in that study. In the apo simulations, the marker distance predominantly ranged between 5.0 Å and 10.2 Å, with only ~1.7% of frames exceeding 7.6 Å, which is the minimum distance observed in the holo trajectory (Figure 2A left, Figure S3). In contrast, the holo simulations showed a broader distribution from 7.6 to 13.3 Å, with a clear peak near 10 Å, consistent with the stabilized β-stacking conformation reported earlier (Figure S3). For subsequent analysis, we used the median Cβ–Cβ distances from the MD simulations as reference thresholds: 6.0 Å (with a probability of 0.4) for the apo state and 10.0 Å (with a probability of 0.2) for the holo state.

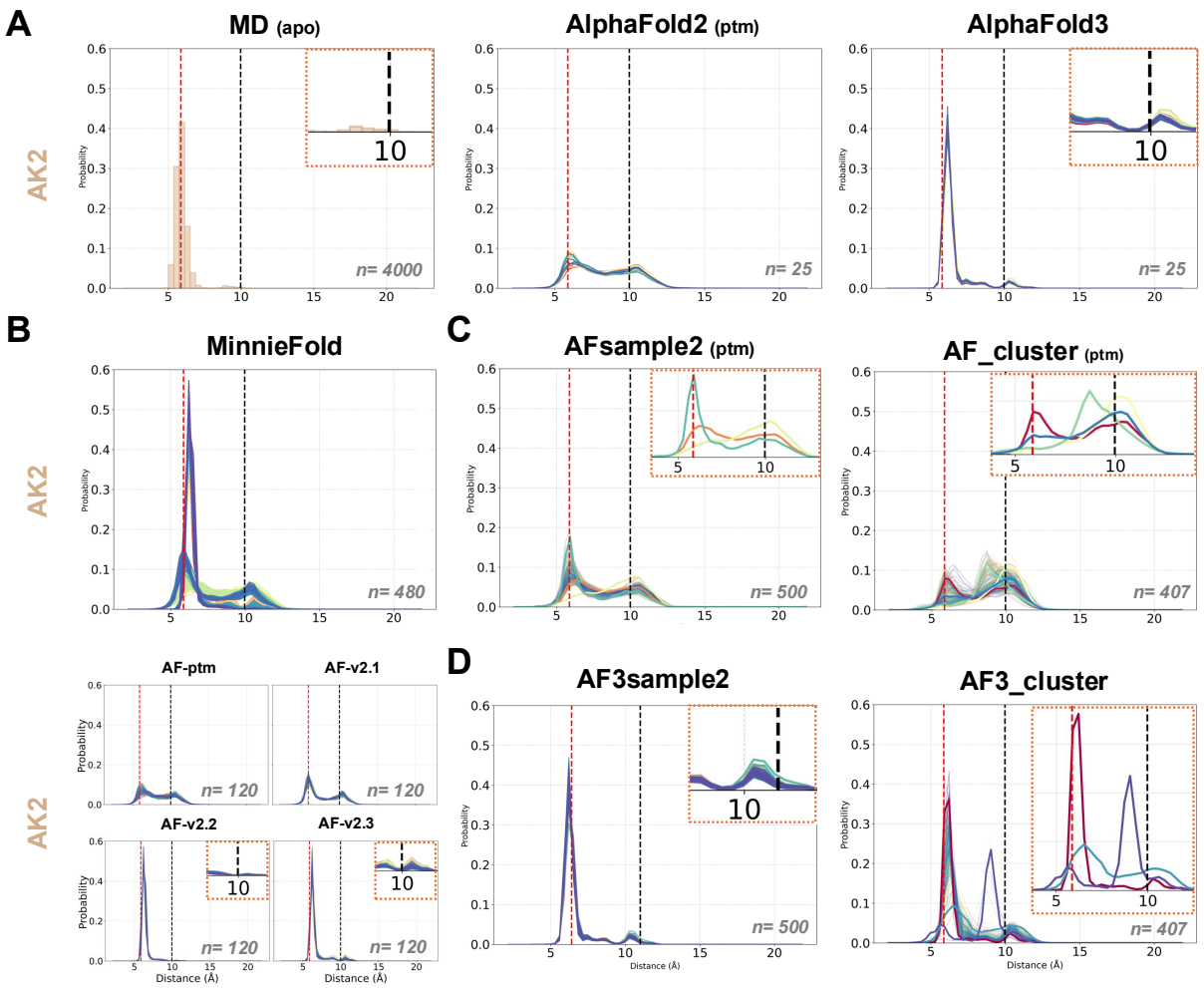

Figure 2. Comparison of marker hinge motion distances for apo AK2. Distogram profiles of the predicted 230-233 marker distance of apo AK2. Left: The measured distance probability distribution, obtained from apo MD simulations. Middle: AF2 distogram for the same pair. Right: AF3 distogram for the same pair. Distogram profiles of 230-233 pair calculated by (**B**) MinnieFold; all (top) and by version (bottom), (**C**) AFsample2 and AF_Cluster, (**D**) AF3sample2 and AF3_cluster. The dashed lines indicate the threshold distances obtained from MD simulations: at 6.0 Å in red for the apo and 10.0 Å in black for the holo state. Close-up views are highlighted with orange dashed frames. The sample given each plot is provided on the panel, indicated with *n*.

Distogram Profile Evaluation Across Different AlphaFold Versions

To assess how accurately different AF versions reflect the binding-induced hinge dynamics captured in our MD simulations, we compared our MD-based marker distance distributions with those predicted by the distograms of AF2 and AF3. For this, we generated 25 independent distance probability distributions by each AI model using the identical MSA inputs to ensure consistent coevolutionary signals without the use of template. The MSA was constructed with MMseqs2 through ColabFold, where the model generation followed

the default settings of AF2.0 monomer (alphafold_ptm) and the latest version of AlphaFold, i.e., AF3 (see Supplementary Text) [44,45]. As an outcome, in the apo state, AF2-ptm generated broad, bimodal distograms with peaks centered near ~6 Å and ~10 Å (Figure 2A, middle). These peaks correspond approximately to the median distances observed in apo and holo MD simulations, respectively. However, the distinction between the two peaks was limited, with the holo-associated peak reaching a probability of no more than 0.1. In contrast, AF3 produced distograms that closely mirrored the apo MD distribution in both peak positions and relative amplitudes, showing a striking agreement with the simulation data (Figure 2A, right).

To further examine how different AF2 enhanced sampling configurations influence distogram outputs, we used our in-house sampling pipeline, MinnieFold, which systematically explores structural variability across four major AF2 versions (ptm, v2.1, v2.2, and v2.3) [46-48]. Inspired by the Massive Sampling approach [25], MinnieFold systematically varies the key AF2 sampling parameters such as the number of recycling steps, dropout settings, and template inclusion. It generates a total of 480 models across all four AF2 versions, enabling broad sampling of structural diversity in a computationally efficient manner (Supplementary Text). In the blind protein complex prediction challenge CAPRI55, we demonstrated that MinnieFold can produce interaction ensembles up to 11.7 Å RMSD variation. In this work, we applied MinnieFold to investigate how enhanced sampling affects distogram outputs, using the same input MSA as in our previous runs. The resulting distance distributions showed a mix of peak profiles, combining features seen in both AF2-ptm and AF3 (Figure 2B-top). When analyzed individually (Figure 2B-bottom), we saw that ptm and v2.1 displayed similar broad bimodal profiles, with v2.1 showing a stronger apo-associated peak, indicating a tendency toward the unbound state. In contrast, v2.2 produced sharply unimodal distributions centered around 6.0 Å, with a high probability (~0.6). Notably, v2.3 reproduced a bimodal distribution closely matching the MD and AF3 profiles. These results suggest that increased sampling through MinnieFold does not introduce new flexibility signals beyond those observed in standard AF2 runs, but it can help amplify existing conformational features already encoded in specific versions.

Distogram Profile Evaluation by Using Different MSA Content

Since parameter tuning alone did not introduce substantial diversity in the distogram outputs of AF2, we examined the influence of the input MSA on the breadth of distograms. For this, we first used AFsample2, which introduces stochasticity upon randomly masking MSA columns to perturb coevolutionary signals [27]. The second approach was AF_cluster, which clusters sequences to build reduced MSAs that represent distinct evolutionary

subspaces [28]. Both strategies were implemented using the AF2-ptm model for consistency. In the case of AFsample2, the overall bimodal character of the distograms was preserved, but the probability of the apo-associated distance peak approximately doubled compared to the original AF2 run (Figure 2C). In contrast, AF_cluster produced a distinct unimodal peak centered around 8 Å with a probability of approximately 0.15, in addition to the original apo and holo peaks observed in AF2 (Figure 2C, right). This intermediate peak may represent a false positive, resulting from reduced MSA depth or limited sequence diversity, or it could reflect a true transition state between the apo and holo conformations. We performed the same protocols with AF3 with the same MSA inputs (Figure 2D, see Supplementary Text). Similar to AF_cluster, clustered MSA in AF3 produced distinct variations in peak positions, whereas column masking did not substantially affect the peak profiles.

The Influence of MSA Pairing and Iterative Refinement on the Distogram Profiles

Since we unexpectedly observed that AF distograms successfully capture binding-induced hinge motion of AK2 from its apo state, we wanted to further investigate how evolutionary information derived from its binding partner would influence AK2's distogram profiles. To this end, we modeled the AIFM1/AK2 complex by using different AF versions. For the complex prediction, MSAs can be constructed either by pairing sequences of interacting proteins to preserve potential coevolutionary signals or by generating separate alignments for each protein partner [49]. To assess how this choice impacts the modeling process, we compared the distogram profiles of different AF2 versions using paired and unpaired MSAs for the AIFM1/AK2 complex (Figure S4).

When AIFM1 evolutionary information was provided as paired sequences, AF2 multimer (v2.1-3) marker distance distograms retained a bimodal character. In contrast, when unpaired MSAs were used, AF2.2 and AF2.3 distograms converged to a unimodal distribution centered around the holo-state median (~10Å) (Figures S2, S4). Interestingly, when MSA is paired, AF2.1 led to a high probability peak around 8Å, the peak distance observed in the case of AF_cluster (Figure 2C). AF2-ptm showed the opposite trend, with unpaired MSAs producing a bimodal distribution and paired MSAs reducing this bimodality toward the holo-state distance. These pairing effects likely arise because AF2-ptm, trained on single-chain inputs, whereas AF2.2-3, trained for complexes. To gain further insight into what drives the transition from bimodal to unimodal distributions, we analyzed how the distograms evolved across recycling iterations. Each recycle updates pair representations based on inter-residue distance predictions, refining the model incrementally. In AIFM1/AK2 complex (Figure S5), the probability density around the holo-associated peak gradually increased with recycling, while the apo-like peak diminished (when AF2-ptm is used). This

progressive shift suggests that the model incrementally refines its internal representation when the binding partner is present, leading to a more stable conformation seen in holo state.

Translation of Distogram Probabilities into Structural Ensembles

While both apo and holo distograms successfully captured the conformational landscape observed in MD simulations for the marker distance, a key question remained: to what extent are these probability distributions are reflected in the final predicted structures? To answer this, we analyzed the marker Cβ–Cβ distance in the structural ensembles generated by each of the previously described methods (Figure 3).

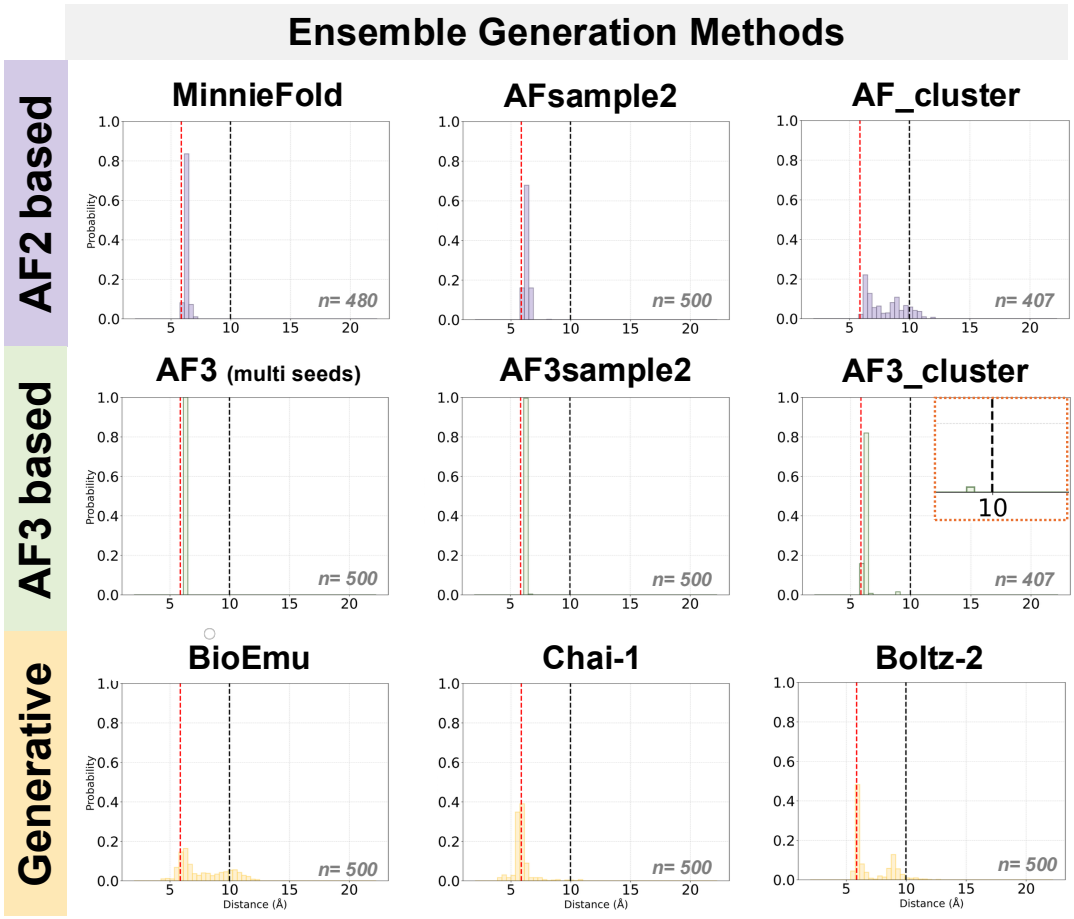

Figure 3. Comparison of marker distance profiles of AlphaFold2, AlphaFold3, and generative model-based sampling methods in capturing conformational diversity of AK2. The dashed lines indicate the threshold distances obtained from MD simulations: at 6.0 Å in red for the apo and 10.0 Å in black for the holo state. The sample given each plot is provided on the panel, indicated with n.

Consequently, the majority of the methods, specifically AF2, MinnieFold, AFsample2, AF3 and AF3sample2 produced predicted structures that exhibit a sharply unimodal distance distribution concentrated tightly around the 6.0 Å apo distance. In contrast, the structural ensembles produced by the MSA clustering strategies did not exhibit this unimodal convergence. Instead, their final distance distributions closely mirrored the corresponding distogram profiles from the naïve runs. AF_cluster outputs spanned a broad, bimodal distribution resembling that of the AF2-ptm distogram, whereas AF3_cluster exhibited a dominant apo-state distance and a minor holo-state population, consistent with its underlying AF3 distogram. We also generated conformational ensembles using BioEmu, Boltz-2, and Chai-1 (see Supplementary Text) to evaluate whether their generative frameworks could more effectively capture conformational diversity [50–52]. All three methods produced significantly broader, bimodal distance distributions, successfully sampling both the apo and holo states. Notably, BioEmu, which integrates AF2-ptm pair embeddings within a diffusion-based framework, yielded ensemble distributions closely matching the AF2-ptm distogram. Interestingly, Boltz-2 produced the ensemble most consistent with the MD-derived distance distribution. Specifically, Boltz-2 uses ensemble-based supervision by integrating multiple samples from experimental ensembles and MD trajectories, suggesting it as a promising alternative in conformational sampling.

Evaluating the Generalizability of Distogram Flexibility Signals

To explore whether our distogram findings extend beyond the AIFM1/AK2 system, we analyzed three additional proteins differing in structural context and flexibility: IL1R1, MIA40, and EIF2B3 (Figure 4). For each protein we generated all-to-all residue distograms with AF2.3 to search for bimodal profiles. IL1R1 is a well-studied receptor that moves between open and closed forms through a hinge-like motion upon binding to its partners (PDB IDs: 1IRA, 1G0Y)[53,54]. The distogram profile in between 133 and 220 residues display two distinct peaks, one at 5.1 Å and another at 10.0 Å, matching the experimentally determined closed and open states (Figure 4A). Though, here, we should note that both the bound and the unbound coordinates of these proteins were seen during the training of all AF versions. Secondly, we analyzed MIA40, another recently resolved interactor of AIFM1. MIA40 does not have a resolved unbound structure. However, it reflects a similar β-sheet stacking when its N-terminus is bound to AIFM1 (PDB ID: 9GQZ)[41]. In this case, the distogram for the N-terminal region did not show multiple peaks, suggesting that this part of the protein might be rigid or a potential motion was not captured by AF (Figure 4B). Interestingly, the monomeric AF2 model already adopted a bound-like conformation as a β-hairpin. The high pLDDT scores in this region may indicate that the β-hairpin is stable on its own and naturally folds into a binding-competent shape, ready for interaction even without its partner. Finally, EIF2B3, as reported in our earlier work, contains a flexible C-terminal

region (residues 446–452) that is missing in all available cryo-EM structures [55]. The distogram of this region also reflected bimodality, suggesting flexibility (Figure 4C). This flexible tail shares a short sequence motif (DQLMEI/DLVMFI) with the C-terminal helix of AK2, hinting at a possible conserved segment that could be linked to functional movement or regulation. Taken together, these examples suggest that AF distograms may be able to capture flexibility patterns across different structural contexts.

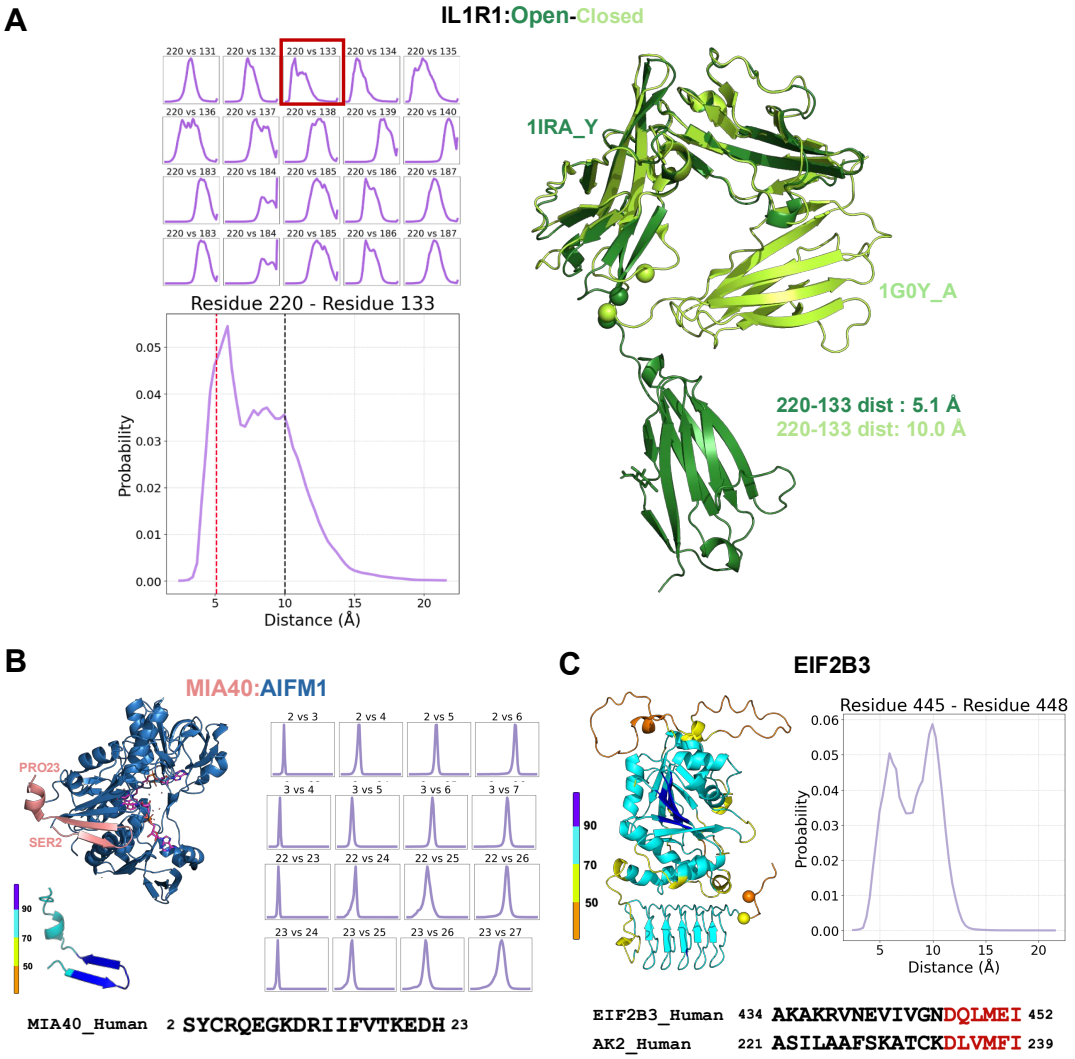

Figure 4. Distogram-based assessment of conformational flexibility across distinct structural contexts (generated by AF2.3): (A) Residue-level distogram profiles of IL1R1 capturing the open-to-closed transition. The right panel shows the corresponding structures for the open (dark green) and closed (light green) conformations, with the measured inter-residue distances. (B) Distogram profiles of MIA40 for the N-terminal residues showing unimodal peaks. (C) Distogram profile for EIF2B3 highlighting the residue 445–448 marker distance. The models are colored by pLDDT, where blue indicates high and orange low confidence. Sequence information at the N-terminal region of MIA40, C-terminal region of EIF2B3, and AK2 is provided under the corresponding panels.

Discussion

In this Perspective article, we investigated whether AF-generated distograms can capture functionally relevant binding-induced hinge motions. For this, we focused on a hinge-driven structural change in AK2 upon AIFM1 binding. Our aim was to assess whether distance probability profiles from distograms reflect the conformational landscape observed in MD simulations and whether they can provide a practical, structure-free indicator of flexibility for cryo-EM map interpretation. Our results demonstrate that both AF2.3 and AF3 distograms for apo AK2 accurately recapitulate the hinge motion at its C-terminal region, closely aligning with MD-derived distance distributions in terms of both peak position and amplitude. At the structural level, the closest matches to the MD distance profiles were observed in the AF3_cluster and Boltz ensembles. To evaluate broader applicability, we extended our distogram analysis to three additional proteins, which supported the potential of AF-derived distograms to detect binding-induced hinge motions, at least across a limited range of systems.

Based on these findings, we hypothesize that the striking agreement between AF2.3/AF3 apo distograms and MD arises as the sequence (by extension, the MSA) should support coevolutionary constraints that encode structural compatibility across distinct conformational states. This in turn should introduce competing evolutionary pressures, where specific residue pairs are required to coevolve in a way that accommodates two alternative distances (e.g., 6 Å and 10 Å for our marker pair). In our case, the MMseqs2-generated MSAs were sufficient enough to capture the MD observation. However, identifying more subtle or transient conformational states for other proteins may require further optimization of the input MSA. Relatedly, Audagnotto et al. demonstrated that MSA generation strategies can significantly impact distogram quality [56]. In their study, they compared different MSA construction methods and assessed the resulting trRosetta distograms. Their results showed that DeepMSA produced more accurate distance distributions for myoglobin, effectively capturing both open and closed state conformations. However, these observations should be revisited by using AF, as distogram generation was not accessible at the time of their study.

Additional approaches like AlphaFlex [57], which combines column masking with predicted residue flexibility, further illustrate how MSAs can be systematically optimized to sample conformational diversity. AlphaFlex estimates residue-level flexibility by integrating structural, evolutionary, and physicochemical features. These flexibility profiles are then used to guide targeted MSA masking, selectively weakening coevolutionary constraints to generate physically plausible conformational states. While the concept is promising, it

could not yet be tested for AK2, as the implementation code is to be unpublished. Finally, probabilistic sampling methods such as BAIes and AlphaFold-Metainference [58-60] also utilize predicted distance distributions as restraints and have shown utility in modeling intrinsically disordered proteins (IDPs), highlighting the growing interest in distogram-based flexibility modeling.

Looking ahead, we suggest that AF distograms can be integrated into cryo-EM workflows as a pre-modeling diagnostic to mark flexible regions before atomic model building. This could help prioritize dynamic domains and guide targeted refinement efforts. A promising direction for future development would involve training strategies that automatically distinguish binding-induced changes from apo conformations. For this, one potential approach would be to identify specific MSA positions responsible for encoding binding-associated flexibility signals in distograms, informed by a systematic analysis of proteins with known bound–unbound landscapes. Though, to realize this potential, AlphaFold's distogram resolution may need refinement. Current limitations, such as the fixed bin size of 0.375 Å and a maximum distance cap around 22 Å, can obscure large-scale transitions. Adaptive binning or fine-tuning strategies could help overcome these constraints and improve the utility of distograms for detecting conformational diversity relevant to cryo-EM interpretation.

Conclusion

Overall, our findings show that while AlphaFold-derived confidence metrics, i.e., as pLDDT, PAE, and pTM, have been widely used to estimate protein flexibility [9,10, 61–65], distograms, which are generated prior to structure prediction, may encode a more fundamental layer of conformational information. Although preliminary, our results suggest that distogram profiles can act as effective, structure-free indicators of binding-induced hinge motions. As such, they hold promise for supporting the interpretation of flexible or partially resolved regions in cryo-EM maps. To enable follow-up studies and reproducibility, all data and scripts used in this work are publicly available at: https://github.com/CSB-KaracaLab/af-distogram-flexibility

Author Contributions

BS: Conceptualization; Investigation; Writing - original draft; Writing - review & editing Methodology; Visualization; Formal analysis.

ABB: Investigation; Formal analysis; Methodology; Writing - original draft.

EK: Writing - original draft; Writing - review & editing; Project administration; Supervision; Conceptualization; Investigation; Methodology; Funding acquisition.

Acknowledgments

This work was supported by the European Molecular Biology Organization (EMBO, grant IG4421) and the Scientific and Technological Research Council of Türkiye (TÜBİTAK, grant 122N790). We also acknowledge the Barcelona Supercomputing Center (BSC) and TÜBİTAK for providing computational resources on the MareNostrum5 supercomputing cluster, which were utilized for the AlphaFold3 runs. We thank the reviewers for their constructive comments and valuable suggestions that helped improve this work.

Conflict of Interest

N/A

REFERENCES

1. Karaca, E., & Bonvin, A. M. (2013). Advances in integrative modeling of biomolecular complexes. Methods (San Diego, Calif.), 59(3), 372–381. https://doi.org/10.1016/j.ymeth.2012.12.004
2. Bullock, J. M. A., Sen, N., Thalassinos, K., & Topf, M. (2018). Modeling Protein Complexes Using Restraints from Crosslinking Mass Spectrometry. Structure (London, England : 1993), 26(7), 1015–1024.e2. https://doi.org/10.1016/j.str.2018.04.016
3. Graziadei, A., & Rappsilber, J. (2022). Leveraging crosslinking mass spectrometry in structural and cell biology. Structure (London, England : 1993), 30(1), 37–54. https://doi.org/10.1016/j.str.2021.11.007
4. Karaca, E., Rodrigues, J. P. G. L. M., Graziadei, A., Bonvin, A. M. J. J., & Carlomagno, T. (2017). M3: an integrative framework for structure determination of molecular machines. Nature methods, 14(9), 897–902. https://doi.org/10.1038/nmeth.4392 5
5. Skalidis, I., Kyrilis, F. L., Tüting, C., Hamdi, F., Chojnowski, G., & Kastritis, P. L. (2022). Cryo-EM and artificial intelligence visualize endogenous protein community members. Structure (London, England : 1993), 30(4), 575–589.e6. https://doi.org/10.1016/j.str.2022.01.001
6. Träger, T. K., Tüting, C., & Kastritis, P. L. (2024). The human touch: Utilizing AlphaFold 3 to analyze structures of endogenous metabolons. Structure (London, England : 1993), 32(10), 1555–1562. https://doi.org/10.1016/j.str.2024.08.018
7. Jumper, J., Evans, R., Pritzel, A., Green, T., Figurnov, M., Ronneberger, O., Tunyasuvunakool, K., Bates, R., Žídek, A., Potapenko, A., Bridgland, A., Meyer, C., Kohl, S. A. A., Ballard, A. J., Cowie, A., Romera-Paredes, B., Nikolov, S., Jain, R., Adler, J., Back, T., ... Hassabis, D. (2021). Highly accurate protein structure prediction with AlphaFold. Nature, 596(7873), 583–589. https://doi.org/10.1038/s41586-021-03819-2
8. Mosalaganti, S., Obarska-Kosinska, A., Siggel, M., Taniguchi, R., Turoňová, B., Zimmerli, C. E., Buczak, K., Schmidt, F. H., Margiotta, E., Mackmull, M. T., Hagen, W. J. H., Hummer, G., Kosinski, J., & Beck, M. (2022). AI-based structure prediction empowers integrative structural analysis of human nuclear pores. Science (New York, N.Y.), 376(6598), eabm9506. https://doi.org/10.1126/science.abm9506
9. Saldaño, T., Escobedo, N., Marchetti, J., Zea, D. J., Mac Donagh, J., Velez Rueda, A. J., Gonik, E., García Melani, A., Novomisky Nechcoff, J., Salas, M. N., Peters, T., Demitroff, N., Fernandez Alberti, S., Palopoli, N., Fornasari, M. S., & Parisi, G. (2022). Impact of protein conformational diversity on AlphaFold predictions. *Bioinformatics*

(Oxford, England), *38*(10), 2742–2748. https://doi.org/10.1093/bioinformatics/btac202

10. Carugo, O. (2023). pLDDT Values in AlphaFold2 Protein Models Are Unrelated to Globular Protein Local Flexibility. Crystals, 13(11), 1560. https://doi.org/10.3390/cryst13111560

11. Del Alamo, D., Sala, D., Mchaourab, H. S., & Meiler, J. (2022). Sampling alternative conformational states of transporters and receptors with AlphaFold2. eLife, 11, e75751. https://doi.org/10.7554/eLife.75751

12. Guo, H. B., Perminov, A., Bekele, S., Kedziora, G., Farajollahi, S., Varaljay, V., Hinkle, K., Molinero, V., Meister, K., Hung, C., Dennis, P., Kelley-Loughnane, N., & Berry, R. (2022). AlphaFold2 models indicate that protein sequence determines both structure and dynamics. Scientific reports, 12(1), 10696. https://doi.org/10.1038/s41598-022-14382-9

13. Tüting, C., Schmidt, L., Skalidis, I., Sinz, A., & Kastritis, P. L. (2023). Enabling cryo-EM density interpretation from yeast native cell extracts by proteomics data and AlphaFold structures. Proteomics, 23(17), e2200096. https://doi.org/10.1002/pmic.202200096

14. Jiang, T., Thielges, M. C., & Feng, C. (2025). Emerging approaches to investigating functional protein dynamics in modular redox enzymes: Nitric oxide synthase as a model system. The Journal of biological chemistry, 301(3), 108282. https://doi.org/10.1016/j.jbc.2025.108282

15. He, Y., Haque, M. M., Stuehr, D. J., & Lu, H. P. (2021). Conformational states and fluctuations in endothelial nitric oxide synthase under calmodulin regulation. Biophysical journal, 120(23), 5196–5206. https://doi.org/10.1016/j.bpj.2021.11.001

16. Tüting, C., Schmidt, L., Skalidis, I., Sinz, A., & Kastritis, P. L. (2023). Enabling cryo-EM density interpretation from yeast native cell extracts by proteomics data and AlphaFold structures. Proteomics, 23(17), e2200096. https://doi.org/10.1002/pmic.202200096

17. Skalidis, I., Kyrilis, F. L., Tüting, C., Hamdi, F., Träger, T. K., Belapure, J., Hause, G., Fratini, M., O'Reilly, F. J., Heilmann, I., Rappsilber, J., & Kastritis, P. L. (2023). Structural analysis of an endogenous 4-megadalton succinyl-CoA-generating metabolon. Communications biology, 6(1), 552. https://doi.org/10.1038/s42003-023-04885-0

18. Skalidis, I., Kyrilis, F. L., Tüting, C., Hamdi, F., Chojnowski, G., & Kastritis, P. L. (2022). Cryo-EM and artificial intelligence visualize endogenous protein community members. Structure (London, England : 1993), 30(4), 575–589.e6. https://doi.org/10.1016/j.str.2022.01.001

19. Kyrilis, F. L., Semchonok, D. A., Skalidis, I., Tüting, C., Hamdi, F., O'Reilly, F. J., Rappsilber, J., & Kastritis, P. L. (2021). Integrative structure of a 10-megadalton eukaryotic pyruvate dehydrogenase complex from native cell extracts. Cell reports, 34(6), 108727. https://doi.org/10.1016/j.celrep.2021.108727

20. Forsberg, B. O., Aibara, S., Howard, R. J., Mortezaei, N., & Lindahl, E. (2020). Arrangement and symmetry of the fungal E3BP-containing core of the pyruvate dehydrogenase complex. Nature communications, 11(1), 4667. https://doi.org/10.1038/s41467-020-18401-z

21. Tüting, C., Kyrilis, F. L., Müller, J., Sorokina, M., Skalidis, I., Hamdi, F., Sadian, Y., & Kastritis, P. L. (2021). Cryo-EM snapshots of a native lysate provide structural insights into a metabolon-embedded transacetylase reaction. Nature communications, 12(1), 6933. https://doi.org/10.1038/s41467-021-27287-4

22. Cui, X., Ge, L., Chen, X., Lv, Z., Wang, S., Zhou, X., & Zhang, G. (2025). Beyond static structures: protein dynamic conformations modeling in the post-AlphaFold era. Briefings in bioinformatics, 26(4), bbaf340. https://doi.org/10.1093/bib/bbaf340

23. Stein, R. A., & Mchaourab, H. S. (2022). SPEACH_AF: Sampling protein ensembles and conformational heterogeneity with Alphafold2. PLoS computational biology, 18(8), e1010483. https://doi.org/10.1371/journal.pcbi.1010483

24. Wallner B. (2023). AFsample: improving multimer prediction with AlphaFold using massive sampling. Bioinformatics (Oxford, England), 39(9), btad573. https://doi.org/10.1093/bioinformatics/btad573

25. Raouraoua, N., Mirabello, C., Véry, T., Blanchet, C., Wallner, B., Lensink, M. F., & Brysbaert, G. (2024). MassiveFold: unveiling AlphaFold's hidden potential with optimized and parallelized massive sampling. Nature computational science, 4(11), 824–828. https://doi.org/10.1038/s43588-024-00714-4

26. Jing B, Berger B, Jaakkola A. (2024) AlphaFold Meets Flow Matching for Generating Protein Ensembles. Rxiv. https://doi.org/10.48550/arXiv.2402.04845

27. Kalakoti, Y., & Wallner, B. (2025). AFsample2 predicts multiple conformations and ensembles with AlphaFold2. Communications biology, 8(1), 373. https://doi.org/10.1038/s42003-025-07791-9

28. Wayment-Steele, H. K., Ojoawo, A., Otten, R., Apitz, J. M., Pitsawong, W., Hömberger, M., Ovchinnikov, S., Colwell, L., & Kern, D. (2024). Predicting multiple conformations via sequence clustering and AlphaFold2. Nature, 625(7996), 832–839. https://doi.org/10.1038/s41586-023-06832-9

29. Sala, D., Hildebrand, P. W., & Meiler, J. (2023). Biasing AlphaFold2 to predict GPCRs and kinases with user-defined functional or structural properties. Frontiers in molecular biosciences, 10, 1121962. https://doi.org/10.3389/fmolb.2023.1121962

30. Heo, L., & Feig, M. (2022). Multi-state modeling of G-protein coupled receptors at experimental accuracy. Proteins, 90(11), 1873–1885. https://doi.org/10.1002/prot.26382

31. Schwarz, D., Georges, G., Kelm, S., Shi, J., Vangone, A., & Deane, C. M. (2021). Co-evolutionary distance predictions contain flexibility information. Bioinformatics (Oxford, England), 38(1), 65–72. https://doi.org/10.1093/bioinformatics/btab562

32. Senior, A. W., Evans, R., Jumper, J., Kirkpatrick, J., Sifre, L., Green, T., Qin, C., Žídek, A., Nelson, A. W. R., Bridgland, A., Penedones, H., Petersen, S., Simonyan, K., Crossan, S., Kohli, P., Jones, D. T., Silver, D., Kavukcuoglu, K., & Hassabis, D. (2020). Improved protein structure prediction using potentials from deep learning. Nature, 577(7792), 706–710. https://doi.org/10.1038/s41586-019-1923-7

33. Greener, J. G., Kandathil, S. M., & Jones, D. T. (2019). Deep learning extends de novo protein modelling coverage of genomes using iteratively predicted structural constraints. Nature communications, 10(1), 3977. https://doi.org/10.1038/s41467-019-11994-0

34. Schildhauer, F., Ryl, P. S. J., Lauer, S. M., Lenz, S., Barlas, A. B., Ouzounidis, V. R., Jeffrey, K., Marcu, D. C., O'Reilly, F. J., Graziadei, A., Stuiver, M., Schmidt, K., Ewers, H., Spahn, C. M. T., Karaca, E., Busch, K. E., Cheerambathur, D., Schwefel, D., & Rappsilber, J. (2025). An NADH-controlled gatekeeper of ATP synthase. Molecular cell, 85(13), 2567–2580.e12. https://doi.org/10.1016/j.molcel.2025.06.007

35. Abramson, J., Adler, J., Dunger, J., Evans, R., Green, T., Pritzel, A., Ronneberger, O., Willmore, L., Ballard, A. J., Bambrick, J., Bodenstein, S. W., Evans, D. A., Hung, C. C., O'Neill, M., Reiman, D., Tunyasuvunakool, K., Wu, Z., Žemgulytė, A., Arvaniti, E., Beattie, C., ... Jumper, J. M. (2024). Accurate structure prediction of biomolecular interactions with AlphaFold 3. Nature, 630(8016), 493–500. https://doi.org/10.1038/s41586-024-07487-w

36. Burkart, A., Shi, X., Chouinard, M., & Corvera, S. (2011). Adenylate kinase 2 links mitochondrial energy metabolism to the induction of the unfolded protein response. The Journal of biological chemistry, 286(6), 4081–4089. https://doi.org/10.1074/jbc.M110.134106

37. Dzeja, P., & Terzic, A. (2009). Adenylate Kinase and AMP Signaling Networks: Metabolic Monitoring, Signal Communication and Body Energy Sensing. International Journal of Molecular Sciences, 10(4), 1729-1772. https://doi.org/10.3390/ijms10041729

38. Formoso, E., Limongelli, V., & Parrinello, M. (2015). Energetics and structural characterization of the large-scale functional motion of adenylate kinase. Scientific reports, 5, 8425. https://doi.org/10.1038/srep08425

39. Snow, C., Qi, G., & Hayward, S. (2007). Essential dynamics sampling study of adenylate kinase: comparison to citrate synthase and implication for the hinge and shear mechanisms of domain motions. Proteins, 67(2), 325–337. https://doi.org/10.1002/prot.21280

40. Whitford, P. C., Gosavi, S., & Onuchic, J. N. (2008). Conformational transitions in adenylate kinase. Allosteric communication reduces misligation. The Journal of biological chemistry, 283(4), 2042–2048. https://doi.org/10.1074/jbc.M707632200

41. Rothemann, R. A., Pavlenko, E., Mondal, M., Gerlich, S., Grobushkin, P., Mostert, S., Racho, J., Weiss, K., Stobbe, D., Stillger, K., Lapacz, K., Salscheider, S. L., Petrungaro, C., Ehninger, D., Nguyen, T. H. D., Dengjel, J., Neundorf, I., Bano, D., Poepsel, S., & Riemer, J. (2025). Interaction with AK2A links AIFM1 to cellular energy metabolism. Molecular cell, 85(13), 2550–2566.e6. https://doi.org/10.1016/j.molcel.2025.05.036

42. 2C9Y X-ray structure, (2005). https://doi.org/10.2210/pdb2C9Y/pdb

43. Barlas, A.B. (2024). Understanding the function of biomolecular complexes through the lens of molecular dynamics. [Doctoral dissertation, Dokuz Eylul University, Izmir]. Source: https://tez.yok.gov.tr/UlusalTezMerkezi/TezGoster?key=E_eEUHQic_C-LvhxNQn1W3wmOCInlBnVAZxdJWqWdN5YkWRUeQ_5_WUDFHGmyRtK

44. Steinegger, M., & Söding, J. (2017). MMseqs2 enables sensitive protein sequence searching for the analysis of massive data sets. Nature biotechnology, 35(11), 1026–1028. https://doi.org/10.1038/nbt.3988

45. Mirdita, M., Schütze, K., Moriwaki, Y., Heo, L., Ovchinnikov, S., & Steinegger, M. (2022). ColabFold: making protein folding accessible to all. Nature methods, 19(6), 679–682. https://doi.org/10.1038/s41592-022-01488-1

46. Savaş, B., Yılmazbilek, İ., Özsan, A., & Karaca, E. (2025). Towards a Greener AlphaFold2 Protocol for Antibody-Antigen Modeling: Insights From CAPRI Round 55. Proteins, 10.1002/prot.26820. Advance online publication. https://doi.org/10.1002/prot.26820

47. Evans R, O'Neill M, Pritzel A, Antropova N, Senior A, Green T, Žídek A, Bates R, Blackwell S, Yim J et al. (2022) Protein complex prediction with AlphaFold-multimer. bioRxiv. https://doi.org/10.1101/2021.10.04.463034

48. https://github.com/google-deepmind/alphafold/blob/main/docs/technical_note_v2.3.0.md AlphaFold v2.3 technical note, released after CASP15.

49. Ozden, B., Kryshtafovych, A., & Karaca, E. (2023). The impact of AI-based modeling on the accuracy of protein assembly prediction: Insights from CASP15. Proteins, 91(12), 1636–1657. https://doi.org/10.1002/prot.26598

50. Lewis, S., Hempel, T., Jiménez-Luna, J., Gastegger, M., Xie, Y., Foong, A. Y. K., Satorras, V. G., Abdin, O., Veeling, B. S., Zaporozhets, I., Chen, Y., Yang, S., Foster, A. E., Schneuing, A., Nigam, J., Barbero, F., Stimper, V., Campbell, A., Yim, J., Lienen, M., ... Noé, F. (2025). Scalable emulation of protein equilibrium ensembles with generative deep learning. Science (New York, N.Y.), 389(6761), eadv9817. https://doi.org/10.1126/science.adv9817

51. Chai Discovery, Boitreaud, J., Dent, J., McPartlon, M., Meier, J., Reis, V., Rogozhnikov, A., & Wu, K. (2024). Chai-1: Decoding the molecular interactions of life. bioRxiv. https://doi.org/10.1101/2024.10.10.615955

52. Passaro, S., Corso, G., Wohlwend, J., Reveiz, M., Thaler, S., Somnath, V. R., Getz, N., Portnoi, T., Roy, J., Stark, H., Kwabi-Addo, D., Beaini, D., Jaakkola, T., & Barzilay, R. (2025). Boltz-2: Towards Accurate and Efficient Binding Affinity Prediction. bioRxiv. https://doi.org/10.1101/2025.06.14.659707

53. Schreuder, H., Tardif, C., Trump-Kallmeyer, S., Soffientini, A., Sarubbi, E., Akeson, A., Bowlin, T., Yanofsky, S., & Barrett, R. W. (1997). A new cytokine-receptor binding mode revealed by the crystal structure of the IL-1 receptor with an antagonist. Nature, 386(6621), 194–200. https://doi.org/10.1038/386194a0

54. Vigers, G. P., Dripps, D. J., Edwards, C. K., 3rd, & Brandhuber, B. J. (2000). X-ray crystal structure of a small antagonist peptide bound to interleukin-1 receptor type 1. The Journal of biological chemistry, 275(47), 36927–36933. https://doi.org/10.1074/jbc.M006071200

55. Circir, A., Koksal Bicakci, G., Savas, B., Doken, D. N., Henden, Ş. O., Can, T., Karaca, E., & Erson-Bensan, A. E. (2022). A C-term truncated EIF2Bγ protein encoded by an intronically polyadenylated isoform introduces unfavorable EIF2Bγ-EIF2γ interactions. Proteins, 90(3), 889–897. https://doi.org/10.1002/prot.26284

56. Audagnotto, M., Czechtizky, W., De Maria, L., Käck, H., Papoian, G., Tornberg, L., Tyrchan, C., & Ulander, J. (2022). Machine learning/molecular dynamic protein structure prediction approach to investigate the protein conformational ensemble. Scientific reports, 12(1), 10018. https://doi.org/10.1038/s41598-022-13714-z

57. Ge, L., Cui, X., Zhao, K., Zhou, X., Zhang, Y., & Zhang, G. (2025). AlphaFlex: Accuracy modeling of protein multiple conformations via predicted flexible residues. bioRxiv. https://doi.org/10.1101/2025.07.11.664327

58. Brotzakis, Z. F., Zhang, S., Murtada, M. H., & Vendruscolo, M. (2025). AlphaFold prediction of structural ensembles of disordered proteins. Nature communications, 16(1), 1632. https://doi.org/10.1038/s41467-025-56572-9

59. Schnapka, V., Morozova, T. I., Sen, S., & Bonomi, M. (2025). Atomic resolution ensembles of intrinsically disordered proteins with Alphafold. bioRxiv. https://doi.org/10.1101/2025.06.18.660298

60. Sen, S., Hoff, S. E., Morozova, T. I., Schnapka, V., & Bonomi, M. (2025). Advancing in silico drug design with Bayesian refinement of AlphaFold models. bioRxiv. https://doi.org/10.1101/2025.06.25.661454

61. Vander Meersche, Y., Diharce, J., Gelly, J. C., & Galochkina, T. (2025). Flexibility or uncertainty? A critical assessment of AlphaFold 2 pLDDT. Structure (London, England : 1993), S0969-2126(25)00344-2. Advance online publication. https://doi.org/10.1016/j.str.2025.09.001

62. Ma, P., Li, D. W., & Brüschweiler, R. (2023). Predicting protein flexibility with AlphaFold. Proteins, 91(6), 847–855. https://doi.org/10.1002/prot.26471

63. Wróblewski, K., & Kmiecik, S. (2024). Integrating AlphaFold pLDDT Scores into CABS-flex for enhanced protein flexibility simulations. Computational and structural biotechnology journal, 23, 4350–4356. https://doi.org/10.1016/j.csbj.2024.11.047

64. Tesei, G., Trolle, A. I., Jonsson, N., Betz, J., Knudsen, F. E., Pesce, F., Johansson, K. E., & Lindorff-Larsen, K. (2024). Conformational ensembles of the human intrinsically disordered proteome. Nature, 626(8000), 897–904. https://doi.org/10.1038/s41586-023-07004-5

65. Jussupow, A., & Kaila, V. R. I. (2023). Effective Molecular Dynamics from Neural Network-Based Structure Prediction Models. Journal of chemical theory and computation, 19(7), 1965–1975. https://doi.org/10.1021/acs.jctc.2c01027